Lasing from Laminated Quasi-2D/3D Perovskite Planar Heterostructures

Yang Li,* Julie Roger, Isabel Allegro, Jan C. Fischer, Qihao Jin, Uli Lemmer, Ian A. Howard,* and Ulrich W. Paetzold*

Planar heterostructures are widely used in commercial III–V semiconductor lasers, but not yet explored for perovskite gain media. This study investigates the gain performance of a $CsPbBr_3(BABr)_x/CsPbBr_3$ (quasi-2D/3D) perovskite planar heterostructure fabricated by lamination. The resulting heterostructure is designed to enhance the photon and excited-state density in a non-quantum-confined thin 3D layer (30 nm) by simultaneously 1) confining the optical mode and 2) supporting excited-state transfer from the wider-bandgap quasi-2D perovskite to the lower-bandgap 3D perovskite. This allows the low amplified spontaneous emission (ASE) threshold of 150 ($\pm$20) μJ cm^{-2} and lasing threshold of 46 ($\pm$15) μJ cm^{-2} to be realized in such a heterostructure under nanosecond pumping. Further modeling reveals that the ASE performance can be significantly improved via maximizing the excited-state transfer efficiency (only 14% for current prototypes) and highlights the potential of perovskite planar heterostructures as high-performance gain media.

1. Introduction

Solution-processed perovskite materials currently receive high attention for lasing applications.[1] Optically pumped lasing was demonstrated using single layer perovskite gain materials in various feedback structures including distributed feedback structures (DFB),[2] vertical cavity surface-emitting laser (VCSEL) architectures,[3] and whispering-gallery mode (WGM) structures.[4] Furthermore, lasing was demonstrated with 3D,[3a] 2D,[5] 1D,[6] and 0D[7] perovskite gain media. The achievement of continuous-wave (CW) lasing,[5,8] optically pumped light-emitting diodes (LEDs),[9] and high-current LEDs[10] demonstrate

Y. Li, J. Roger, J. C. Fischer, U. Lemmer, I. A. Howard, U. W. Paetzold
Institute of Microstructure Technology
Karlsruhe Institute of Technology
Hermann-von-Helmholtz-Platz 1
76344 Eggenstein-Leopoldshafen, Germany
E-mail: yang.li2@kit.edu; ian.howard@kit.edu; ulrich.paetzold@kit.edu
Y. Li, J. Roger, I. Allegro, Q. Jin, U. Lemmer, I. A. Howard, U. W. Paetzold
Light Technology Institute
Karlsruhe Institute of Technology
Engesserstrasse 13, 76131 Karlsruhe, Germany

progress toward realizing lasing in a perovskite gain material under electrical injection.[11]

Multilayer heterostructures ensure a high local concentration of charge carriers and are key for electrically pumped commercial lasers, with III–V semiconductor lasers a key enabling device for optical communications.[12] In analogy, the high-performance perovskite gain materials reported in literature also exhibit concentration of excited states by energy transfer of optical excitations due to non-homogeneous energy landscapes. For example, quasi-2D perovskites exhibit random distributions of quantum wells with different bandgaps in a type I heterostructure, in which excited states must funnel into the lower energy wells.[13]

It was in such a structure that the first demonstration of room temperature CW lasing[5] in the field of perovskite lasers was made in 2020. Similarly, low temperature ($T \approx 100$ K) CW lasing[8] was also observed in the orthorhombic phase of MAPbI$_3$ 3D perovskite with randomly distributed low bandgap tetragonal-phase inclusions generated by local heating of the pump laser. Both examples therefore suggest that utilizing type I heterostructures to concentrate excited states in a smaller volume of the film may be important for achieving CW lasing in perovskites. These "bulk heterostructure type" perovskites represent randomly mixed-phase systems; and inspired our study of planar and ordered multilayer perovskite heterostructures of type I band alignment to control such energy transfer for lasing applications.

The creation of perovskite/perovskite planar heterostructures using sequential solution-based processing methods is a major challenge, due to material interdiffusion and a lack of suitable orthogonal solvent systems.[14] The solution-based deposition of quantum dot heterostructures[15] is possible, but processing a stack of planar 2D or 3D perovskite heterostructures in this way is still challenging. To solve this, lamination of two complementary half stacks is established as a method providing the flexibility of combining two separately processed perovskite layers for photovoltaic applications,[16] although here a type II band alignment to promote charge separation is targeted.

The planar heterostructures in this work are fabricated by thermally laminating (100 °C and 80 MPa) a wider-bandgap CsPbBr$_3$(BABr)$_x$ layer onto a lower-bandgap CsPbBr$_3$ layer. The heterostructure exhibits type I band alignment to support the excited-state transfer, which is confirmed by the femtosecond
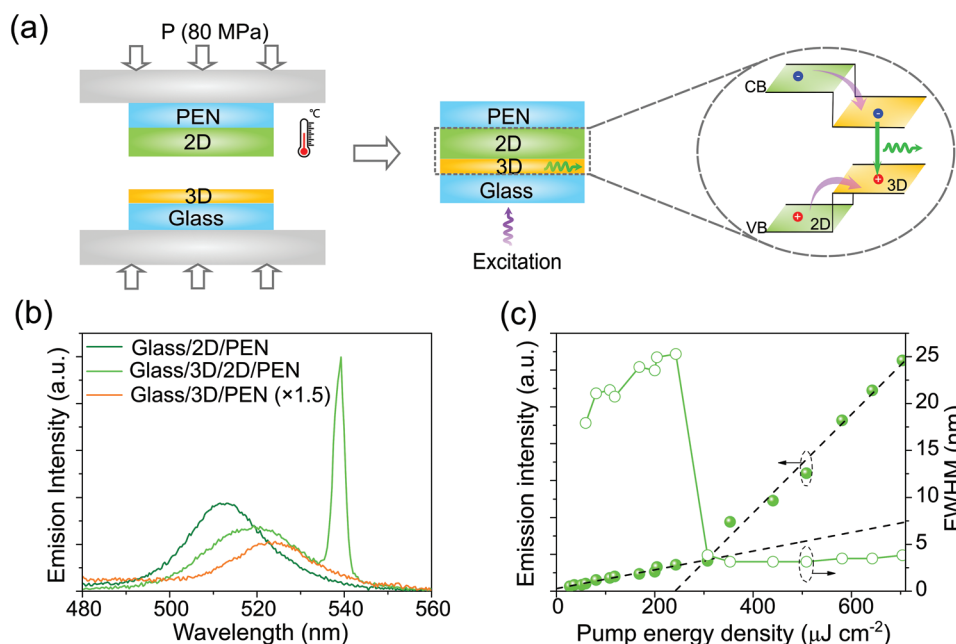
Figure 1. ASE in 2D/3D perovskite planar heterostructure. a) Schematic of the lamination process (left), the laminated full film stack (middle), and the type I band alignment of the formed $CsPbBr_3(BABr)_{0.6}/CsPbBr_3$ (2D/3D) perovskite heterostructure that facilitates the excited-state transfer (right). b) Emission spectra at the excitation power of 580 µJ cm^{-2} (355 nm, 1 kHz, 1.1 ns pulse length) for the stacks of Glass/2D/PEN, Glass/3D/2D/PEN, and Glass/3D/PEN. All the samples are processed using the same lamination process parameters to ensure comparability. The layer thickness of 3D and 2D films is 40 and 90 nm, respectively. For better comparison, the PL spectrum of Glass/3D/PEN sample is magnified 1.5 times. c) Plots of emission intensity and FWHM versus the pump energy densities. The black dashed lines are the linear fits before and after the ASE signature appears.

transient absorption (fs-TA) measurement. The present study of amplified spontaneous emission (ASE) in the heterostructure as a function of the $CsPbBr_3$ layer thickness supports the hypothesis of energy transfer. Furthermore, a VCSEL based on the planar heterostructure demonstrates a respectable threshold of 46 (±15) µJ cm^{-2} despite the non-optimal energy transfer in these heterostructures. Given the room for improvement of the excited-state transfer efficiency, the concept of using perovskite heterostructures for lasing is expected to yield even lower lasing thresholds than single-layer gain media in future.

2. Results and Discussion

2.1. Lamination of the Quasi-2D/3D Planar Heterostructure

The perovskite planar heterostructure is fabricated by thermally laminating a flexible polyethylene naphthalate (PEN) foil with $CsPbBr_3(BABr)_{0.6}$ (quasi-2D perovskite) layer onto a high-temperature-annealed $CsPbBr_3$ (HTA-3D perovskite)[17] layer (see **Figure 1**a). To form a proper junction, a lamination process that involves a lamination step at elevated temperature (70 °C) and high pressure (80 MPa) for 5 min is pursued (see Experimental Section). For convenience, the quasi-2D perovskite and HTA-3D perovskite are abbreviated as 2D and 3D in the following. We note that during the lamination process the integrity of the 3D layer is maintained and no intermixing of the 2D and 3D layers occurs (Figures S1 and S2, Supporting Information). The 2D/3D planar heterostructure exhibits a type I (straddling gap) band alignment[18] as desired for an energy cascade

structure to realize excited state transfer from the wider-bandgap 2D perovskite to the lower-bandgap 3D perovskite layer.

To introduce the concept of the perovskite planar heterostructure, Figure 1b compares the emission spectra acquired from the 2D single layer (90 nm), the 3D single layer (40 nm), and the 2D/3D heterostructure at excitation fluence of 580 µJ cm^{-2} (355 nm and 1.1 ns pulse length). For fair comparison, the 2D (or 3D) single layers also underwent the same lamination step (see Figure S3, Supporting Information). The photoluminescence (PL) spectra with a maximum at 522 nm (513 nm) for the 3D (2D) single layer agrees with the expected behavior for type I alignment as illustrated in Figure 1a. The 2D/3D heterostructure exhibits a slightly broader emission spectrum with a maximum at 520 nm and the broad PL spectrum appearing like the superposition of the single layer PL signals and suggesting incomplete energy transfer. The energy transfer with type I alignment can be further supported by the PLQY (PL quantum yield) measurements (see Figure S4, Supporting Information). On top of the broad PL spectrum, a pronounced narrow band is observed, which we attribute to ASE. Interestingly, the narrow ASE band (at 540 nm) is only apparent in the heterostructure. This ASE peak originates from the 3D layer of the heterostructure as the peak energy matches that of the thick 3D single layers (90 nm).[17] An ASE threshold of 300 (±45) µJ cm^{-2} is determined for this heterostructure based on light-in light-out relation and the full width half maximum (FWHM) of the emission peak (see Figure 1c). Although the ASE threshold of this example 2D/3D heterostructure is still higher as compared to the ASE of best performing thick 3D single layers (90 nm),[17] it is important
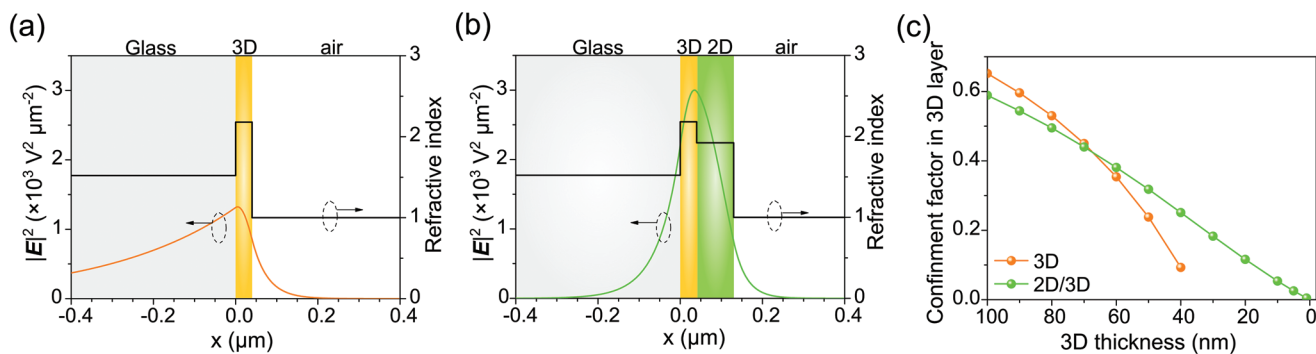
Figure 2. Optical confinement in 2D/3D perovskite heterostructures. a,b) Calculated square of the electric field ($|E|^2$) for the TE_0 mode and refractive index (Figure S5, Supporting Information) profile of a) the 3D perovskite single layer and b) the 2D/3D perovskite heterostructure sandwiched between glass and air capping layers. The integral along the x-axis of the longitudinal component of the Poynting vector is normalized to 1 W μm^{-1} (power per lateral unit length in γ-direction).[19] c) Optical confinement factor in the 3D layer versus with the 3D layer thickness. The 2D layer thickness is fixed at 90 nm.

to note that even this initial configuration outperforms the counterpart sample with similar 3D single layers thickness (40 nm) and further room for improvements is explored in the following.

Next, we elaborate on the presence of the ASE signature in the heterostructure versus its absence in the single layer. It can be attributed to 1) improved optical confinement and 2) slightly enhanced excited-state densities in the thin 3D layer due to excited-state transfer. There is significant potential to increase the excited-state transfer and thereby improve gain performance.

2.2. Optical Confinement in the Heterostructure

One advantage of the 2D/3D heterostructure is the ability to sustain a high portion of the optical mode in the thin 3D layers. **Figure 2**a,b shows the profile of the squared electric field ($|E|^2$) for the TE_0 waveguide mode in our 3D single layer and the 2D/3D heterostructure, respectively.[19] A much higher $|E|^2$ is apparent in the 3D layer of the heterostructure compared to the corresponding 3D single layer. This leads to a significantly enhanced optical confinement factor (defined as the ratio of $|E|^2$ restricted in the interested region) in a 40 nm 3D layer in a heterostructure (25%) versus a 3D single layer (9%). Figure 2c reveals the roughly linear loss of the optical confinement factor with decreasing the 3D layer thickness in the heterostructure. Increasing the carrier density in the 3D layer by energy transfer from the 2D layer will lead to a higher rate of photon emission (and therefore a higher photon density). As the rate of free charge carrier emission scales quadratically with density,[17] the increased carrier densities in thinner 3D layers can compensate for the loss due to poorer confinement and lead to better net ASE performance in thinner films as discussed below.

2.3. Excited-State Transfer in the Heterostructure

A key asset of the proposed 2D/3D heterostructure is the excited states transfer from the 2D layer to the 3D layer leading to excited states accumulation in the 3D gain medium. Fs-TA measurements demonstrate energy transfer in these

structures. **Figure 3**a compares the TA contour plots of the single layers and the corresponding heterostructure acquired at low excitation fluence (0.5 μJ cm^{-2}). A narrow bleaching band close to the absorption band edge is apparent from the TA spectrum centering at 511 nm and 521 nm for 2D and 3D single layer, respectively. Consequently, a wider bleaching band reflecting the contribution from both the 2D and 3D layers is apparent for the heterostructure (see Figure S6, Supporting Information). The TA dynamics of the 2D layer (at 511 nm) and 3D layer (at 521 nm) change after laminating them together. Compared to the 2D single layer, a faster excited-state decay is observed for the 2D contribution in the 2D/3D heterostructure (Figure 3b). This indicates the quenching of excited states in the 2D layer by transfer to the 3D layer of the heterostructure. Fitting the dynamics with a single exponential decay function, lifetimes of 3658 (±15) ps and 2900 (±11) ps for the 2D single layer and the 2D layer in the heterostructure are found. The fraction of excited-state transfer can be estimated at 21% with the transfer rate of 7.1×10^7 s^{-1}. Given that the pulse length during excitation of ASE is 1.1 ns, only 30% of the excited-state population decays within this time scale. This results in a transfer efficiency of only 6% (within 1.1 ns) relevant for ASE (see Supplementary note 1, Supporting Information), which certainly leaves a large room for improvement. Most importantly, compared to the 3D single layer, a slower excited-state decay is apparent for the heterostructure (Figure 3c), suggesting higher carrier densities (proportional to the TA signal) in the lower-bandgap 3D layer of the heterostructure due to a transfer from the 2D layer. This observation supports the hypothesis of excited-state transfer from 2D layer to 3D layer but indicates that there is significant room for improvement. We note that the defect passivation of the 2D layer laminated on top of 3D layer might also contribute to the long lifetimes (>2 ns) of the 3D film. (See Figure S7, Supporting Information).

To test the hypothesis whether the transfer efficiency inversely correlates with the ASE threshold, the excited-state transfer in our 2D/3D heterostructure is manipulated by adjusting the BABr amount in the CsPbBr$_3$(BABr)$_x$ 2D perovskite layer. As demonstrated in our previous study,[17] by reducing the BABr amount, the averaged quantum well depth in the quasi-2D perovskite increases, which results in a lower bandgap and
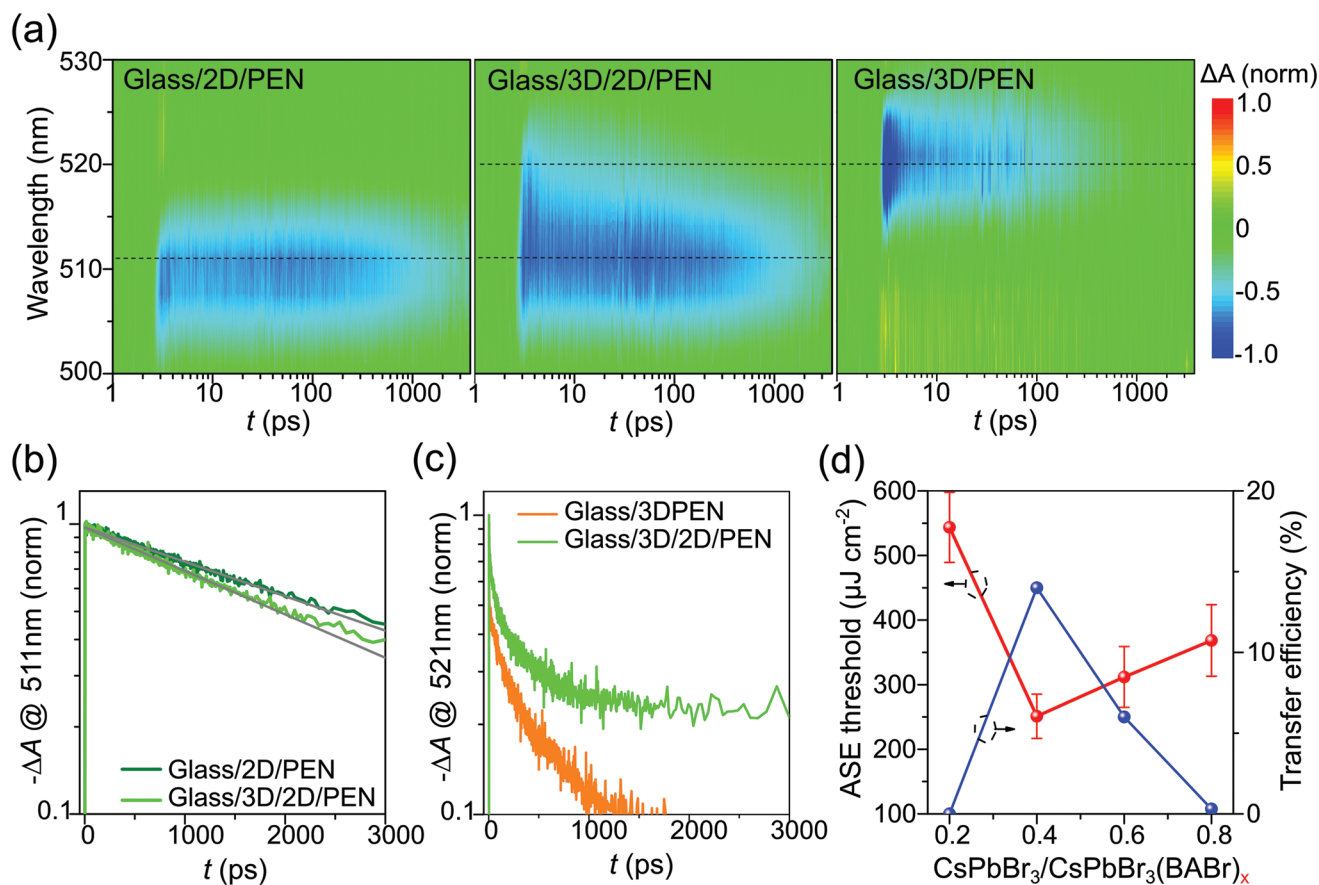
Figure 3. Excited-state transfer from 2D layer to 3D layer and its effect on ASE performance. a) Normalized fs-TA spectra of Glass/2D/PEN (left), Glass/2D/3D/PEN (middle), and Glass/3D/PEN (right) films acquired under laser excitation at 405 nm (260 fs, 1 kHz) and pump energy density of 0.5 μJ cm^{-2}. ΔA represents the TA signal. b,c) Normalized bleaching dynamics at b) 511 and c) 521 nm. The gray lines are the fits using a single exponential decay function. All the spectra are obtained in vacuum by excitation via the PEN side. d) ASE threshold and the excited-state transfer efficiency of the 2D/3D heterostructure versus the BABr content in the 2D layer.

an increase of the conductivity. A minimum ASE threshold of 250 (±27) μJ cm^{-2} is determined for a reduced BABr amount of 0.4 (see Figure 3d). In line with our hypothesis, the transfer efficiency relevant for ASE exhibits a maximum of 14% with a transfer rate of 1.2×10^8 s^{-1} (see Figure S8, Supporting Information). We hypothesize that the increase in excited-state transfer benefits from the increased diffusion in the CsPbBr$_3$(BABr)$_{0.4}$ perovskite compared to the investigated stoichiometry with higher BABr content of 0.6 investigated above. However, further reducing the spacer content beyond the optimum condition leads to a too small bandgap difference between the quasi-2D layer and the 3D layer, which counteracts the desired excited-state transfer (Figure S8h, Supporting Information). Another route to modify the excited-state transfer are the lamination parameters. As shown by optimizing the lamination parameters (Figure S9, supporting information) the ASE threshold of the heterostructure decreases to 150 (±20) μJ cm^{-2} (100 °C for 15 min), which is attributed to the improved interfacial contact facilitating the excited-state transfer. Overall, these results highlight the direct inverse correlation of the exited-charge transfer efficiency and the ASE threshold in the 2D/3D heterostructures.

2.4. Enhancing Excited State and Quantum Confinement in the Heterostructure

Another key handle to manipulate the excited-state confinement is the thickness of the 3D layer in the heterostructure. For a single 3D layer, the optical confinement decreases with decreasing layer thickness (Figure 2c) and the excited state density remains similar, leading to a significant increase of ASE threshold (see **Figure 4**a). In contrast, the ASE threshold of the heterostructure remains constant as the 3D layer thickness decreases to 30 nm. This illustrates that the modest loss in optical confinement must be compensated by an increase in the emission rate due to an increase in the carrier density within the 3D layer of the heterostructure. Below 30 nm, the ASE threshold of the heterostructure is found to increase and the ASE peak blueshifts (see Figure S10, Supporting Information). Examining the absorption band edge and PL peak of the 3D single layer reveals quantum confinement (including weak and strong confinements, see Figure S11, Supporting Information) in the thin 3D layer (<30 nm) as evident by the increased bandgap (Figure 4b) of the 3D film with decreasing the film thickness. Moreover, the PL$_0$ slope[17] (the power exponent for excitation

**ADVANCED
SCIENCE NEWS**

www.advancedsciencenews.com

**ADVANCED
FUNCTIONAL
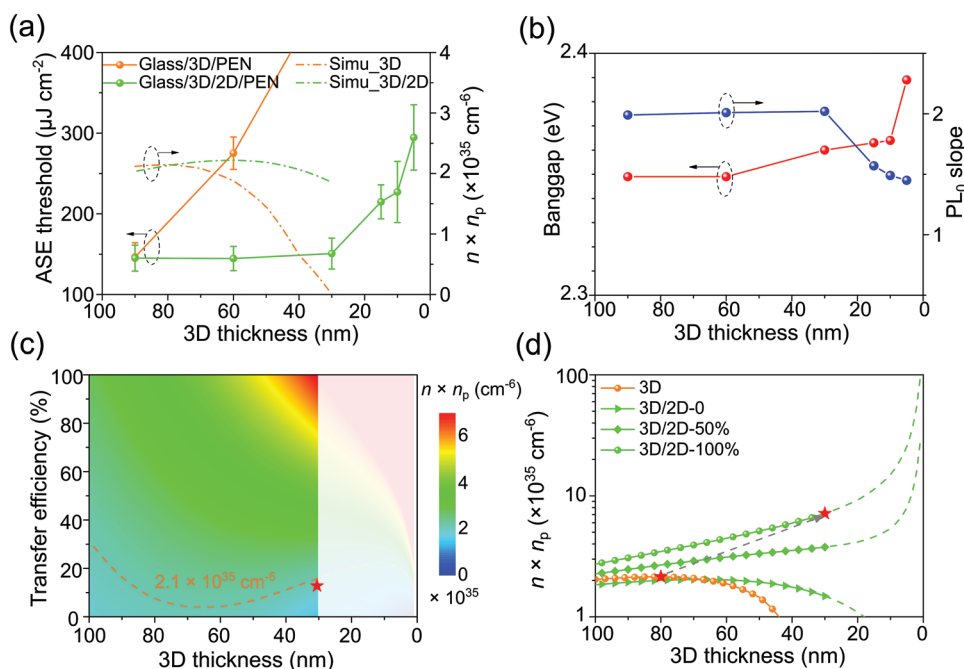MATERIALS**

www.afm-journal.de

Figure 4. Enhancing excited-state and quantum confinement in the heterostructure. a) ASE threshold and the modeled product ($n \times n_p$) of excited-state density and photon density for the 3D layer and the 2D/3D heterostructure (10% transfer efficiency). b) Bandgap and PL_0 slope of the 3D single layer. c) Modeled $n \times n_p$ of the 3D layer of the 2D/3D heterostructure. The excitation level is set to 1×10^{13} cm^{-2}. The orange dashed contour line calculated based on the $n \times n_p$ value of the best performing thick 3D single layer (90 nm). It is seen that a higher transfer efficiency is needed when the non-optimal thickness of the 3D layer is chosen. The red star represents the $n \times n_p$ of the heterostructure (30 nm for 3D and CsPbBr$_3$(BABr)$_{0.4}$ for 2D). d) Comparison of the $n \times n_p$ between the 2D/3D heterostructure with varying transfer efficiencies and the 3D single layer counterpart. The red stars indicate the maximum value of $n \times n_p$ for 3D single layer (2.1×10^{35} cm^{-6}) and 2D/3D heterostructure (7.2×10^{35} cm^{-6}).

fluence dependence of initial transient PL signal) decreases for decreasing 3D layer thicknesses (Figure 4b). This indicates that the emissive species of the 3D film shifts from pure free carrier (slope = 2) to a combination of the free carrier and exciton (slope = 1) with decreasing the 3D film thickness. The quantum confinement-induced excitonic character is also confirmed by the increased brightness of the thin 3D films (<30 nm) under a UV lamp (low excitation density, Figure S11c, Supporting Information). Since the nonradiative loss of exciton–exciton annihilation[17] at the high excitation level in the quantum confined 3D films is detrimental, the ASE threshold of the heterostructure with a thin 3D layer (<30 nm) increases.

To assess the potential of optimized 2D/3D heterostructure and future type I multilayer heterostructures as the gain medium for lasing, the product of the excited-state density and the photon density ($n \times n_p$) in the 3D layer is modeled (see supplementary note 2, Supporting Information). The higher $n \times n_p$, the lower the ASE threshold. Key handles are the excited-state transfer efficiency and the 3D layer thickness. The surface roughness-induced scattering losses are not considered in the simulation as the roughness is not severely affected by the lamination step (see Figure S12, Supporting Information). The model is not valid in the quantum confined regime (3D layer thickness <30 nm) due to the fact that we only consider free carrier emission. As shown in Figure 4c, with lower 3D layer thickness and higher excited-state transfer efficiency the $n \times n_p$ increases, and this indicates a lower ASE threshold. However, for low transfer efficiencies (e.g., <30%), there is an optimal thickness below

which the $n \times n_p$ product begins to decrease. The reason is that the reduced optical confinement (Figure 2c) in the thinner 3D layers cannot be compensated anymore by increased excited-state densities if the excited-state transfer efficiency is poor. The latter aspect is illustrated in Figure 4d. For the 3D single layer, $n \times n_p$ reaches the maximum at the thickness of 80 nm, as the compromise between the loss in optical confinement factor (Figure 2c) and the enhancement in excited-state density (Figure S13, Supporting Information) is best for this thickness. The maximum shifts to thinner 3D film (68 nm) with a lower $n \times n_p$ maximum (indicating worse ASE performance) for the heterostructure with negligible excited-state transfer occur (Figure 4d). When excited-state transfer is 100%, the $n \times n_p$ of the heterostructure becomes significantly enhanced. The calculated maximum value of $n \times n_p$ for the heterostructure is more than three times higher than for the 3D single layer (highlighted by the red stars in Figure 4d), which indicates the potential to further improved ASE performance of the 2D/3D heterostructure. Finally, the $n \times n_p$ of the heterostructure as a function of 3D film thickness for 10% efficient energy transfer at the same time as the ASE threshold is shown in Figure 4a. The experimentally measured ASE threshold and the $n \times n_p$ remain almost constant over the range of film thickness, as the increase in the carrier concentration with decreasing film thickness only compensates for the decreasing optical confinement at this low energy transfer efficiency. In this sense, the experimental results on the ASE threshold as a function of film thickness are in good agreement with the transfer efficiency found above.
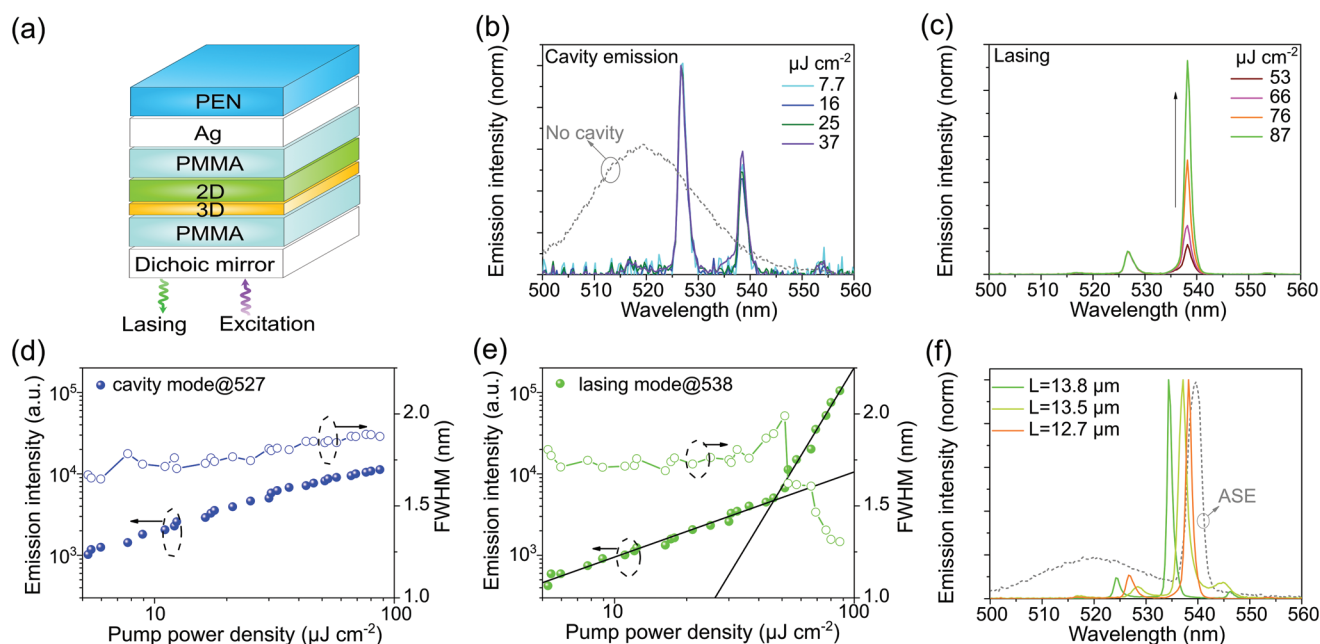
Figure 5. Lasing in CsPbBr$_3$(BABr)$_{0.4}$/CsPbBr$_3$ perovskite heterostructure. a) Schematic illustration of the Fabry-Perot resonator comprising two parallel planar reflectors (a dichroic mirror and a silver film), 2D (90 nm)/3D (30 nm) heterostructure gain medium, and the PMMA interlayers. b,c) Normalized emission spectrum as a function of pump energy density b) below and c) over lasing threshold. The gray dashed line in b) indicates the emission spectra without a cavity. d,e) Emission intensities and FWHM of d) the cavity mode at 527 nm and e) the lasing mode at 538 nm as a function of pump power densities. f) Lasing spectrum from different batches of the samples using the same processing parameters shows different effective cavity length. The gray dashed line indicates the ASE spectrum from the corresponding heterostructure.

2.5. VCSEL Comprising a Perovskite Heterostructure

Finally, a VCSEL based on the 2D/3D heterostructure is realized (see **Figure 5**a). The vertical cavity of the VCSEL is defined by a dichroic mirror (Thorlabs, DMSP425T) with a reflectivity over 99% (500–700 nm) and a metallic Ag thin film reflector (150 nm). The cavity spacer (PMMA layer) and the perovskite gain medium are subsequently deposited onto the reflectors. To complete the VCSEL the two stacks of the CsPbBr$_3$(BABr)$_{0.4}$/PMMA/dichroic and CsPbBr$_3$/PMMA/Ag/PEN film are then laminated together. We note that the PMMA spacer is used to avoid the PL quenching of the CsPbBr$_3$ film by the Ag thin film and shows no influence on the ASE performance (see Figure S14, Supporting Information). Upon pulsed excitation at 355 nm (1.1 ns pulse length), lasing from the perovskite heterostructure VCSEL is demonstrated (Figure 5b–e). At low excitation power (<37 μJ cm^{-2}), two dominant cavity modes (527 and 538 nm) are apparent (see Figure 5b). The effective cavity length (L_{eff}) is estimated as 12.7 μm using the mode spacing ($\Delta\lambda$) based on the equation $L_{eff} = \lambda^2/(2\Delta\lambda)$.[20] At high excitation energy densities (>53 μJ cm^{-2}, Figure 5c), the mode at 538 nm dominates over the mode at 527 nm. The intensity of the lower energy mode (538 nm) shows the expected super-linear increase accompanied by a decrease of the FWHM for pump energy increase >40 μJ cm^{-2} (Figure 5e). In contrast, no lasing is apparent from the mode at 527 nm (Figure 5d). Thus, our 2D/3D heterostructure VCSEL shows single-mode lasing with the threshold of 46 (±15) μJ cm^{-2} that is comparable with the lasing threshold of other perovskite VCSELs reported in the literature (Figure S15 and Table S1, Supporting Information). In addition, a slight change in the lasing wavelength from different batches of the samples is observed, as shown in Figure 5f and Figure S16 (Supporting Information). This is attributed to the change in the effective cavity length induced by the unintentional variation of the film thickness (mainly originating from the PMMA layer). Significantly, the demonstration of the VCSELs with a low lasing threshold encourages the further development and engineering of the perovskite planar heterostructure with improved charge transfer to be an even higher performance gain medium.

The quasi-2D/3D perovskite planar heterostructure is fabricated via a novel lamination process, and the light amplification (both ASE and lasing) is demonstrated in such a heterostructure gain medium. For a given 3D layer thickness, the ASE of the 2D/3D heterostructure consistently exceeds the ASE of the 3D single layer, highlighting the overall superior performance of the 2D/3D heterostructure. However, it should be noted that yet the lowest ASE threshold of the presented 2D/3D heterostructure (150 (±20) μJ cm^{-2}) is in pair with the best performing 3D single layer (90 nm film in Figure 4a). Yet the ASE performance of our 2D/3D heterostructure is limited by a low transfer efficiency of only 14% that leaves significant room for improvements in future (see red star in Figure 4c). Thus, as also apparent from further analysis of $n(t) \times n_p(t)$ (Figure S17, Supporting Information), a faster transfer rate from 2D to 3D layer will lead to a higher instantaneous peak density of carriers and photons in the 3D layer and better ASE performance. Suggested routes to improve the excited-state transfer are 1) improving

**ADVANCED
SCIENCE NEWS**

www.advancedsciencenews.com

**ADVANCED
FUNCTIONAL
MATERIALS**

www.afm-journal.de

the diffusion in the 2D perovskite by modifying the type of the 2D spacer or by improving the out-of-plane alignment of the inorganic sheet; and 2) replacing the 2D perovskite with a 3D perovskite of suitable band alignment. Furthermore, designing more complex multilayers composed of multiple heterostructures (Figure S18, Supporting Information), e.g., a 2D/3D/2D layer sequence can potentially achieve much better ASE performance in the future.

3. Conclusion

This study reports on the first realization of a multilayer perovskite heterostructure gain media with type I energy cascade architecture as a route for achieving high-performance lasing. The planar heterostructure is fabricated by thermally laminating (at 100 °C and 80 MPa) a quasi-2D $CsPbBr_3(BABr)_x$ layer onto a 3D $CsPbBr_3$ layer. The quasi-2D/3D heterostructure realizes simultaneously 1) confining the electrical field enhancement of the optical mode to a very thin 3D layer and 2) supporting excited-state transfer from the wider-bandgap quasi-2D perovskite material to the lower-bandgap 3D perovskite gain material. ASE thresholds as low as 150 (±20) μJ cm^{-2} are measured from this heterostructure that are comparable to best performing thick 3D perovskite single layer (90 nm). Employing fs-TA measurement, the excited-state transfer from the wider-bandgap quasi-2D layer to the lower-bandgap 3D layer is proved and the transfer efficiency relevant for lasing is approximated as 14%. By enhancing the transfer efficiency in the future, the ASE threshold is expected to decline significantly. Moreover, the quasi-2D/3D heterostructure should be considered only as a first step toward more complex multilayer perovskite heterostructure gain media. To demonstrate the technological relevance already at this stage, the first perovskite planar heterostructure laser with a low lasing threshold of 46 (±15) μJ cm^{-2} under 1.1 ns pulse laser excitation is presented.

4. Experimental Section

Perovskite Film and 2D/3D Heterojunction Fabrication: The perovskite precursor solutions with the stoichiometry of $CsPbBr_3(BABr)_x$ dissolved in DMSO were prepared according to the procedure described in the previous paper.[17] The solutions were spin-coated on dedicated substrates at 1000 rpm for 20 s (ramp rate 200 rpm s^{-1}) and 4000 rpm for 40 s (ramp rate 200 rpm s^{-1}). Subsequently, the film was annealed at 70 °C for 15 min (quasi-2D perovskite) and 150 °C for 10 min (3D perovskite). A lamination step (describe in detail below) was finally carried out to complete the 2D/3D heterostructure. Since the PEN could not bear the temperature of 150 °C, the 3D perovskites were only deposited onto glass substrate, and the quasi-2D perovskites are only deposited onto PEN substrate.

VCSEL Fabrication: To fabricate the VCSEL, Ag (150 nm) was first thermally evaporated onto the PEN substrate. The solution of PMMA (350 K, Sigma Aldrich) dissolved in chlorobenzene at 40 mg mL^{-1} was separately spin-coated (6000 rpm for 60 s, ramp rate 1000 rpm s^{-1}) onto the short pass dichroic mirror (DMSP425T, Thorlabs) and above PEN/Ag substrate, which was followed by a drying step at 60°C for 5 min. The quasi-2D and 3D perovskite layers were then separately deposited onto above PMMA/dichroic mirror and PMMA/Ag/PEN substrate. The VCSEL was finally fabricated by laminating the two separate stacks together at 80 MPa and 100 °C for 15 min.

Lamination Process: The lamination was realized with an in-house developed hot embossing machine.[16d] The machine was composed of an upper and a lower tool mounted on a fixed and a movable crossbar respectively, with an integrated heating and cooling unit, a vacuum chamber, and a drive unit. The two independently prepared layer stacks were placed on the machine plate such that the 2D and 3D perovskites face each other. In addition, a Teflon-coated silicon wafer was interposed between the PEN foil and the plate for a uniform pressure distribution. The lamination process can be divided into three main steps: 1) the machine plates and samples were first heated, while the chamber was successively evacuated and flushed with nitrogen to reduce moisture and oxygen in the vacuum chamber; 2) when the temperature of 70 °C (or 100 °C) was reached, a pressure of 80 MPa was applied for a duration of 5 min (or 15 min); 3) the sample was cooled to 40 °C and the pressure was released. After lamination, the 2D/3D were bonded together, and the sample was ready to be characterized.

ASE and Lasing Measurement: The samples were excited from glass side or dichroic mirror side by a diode-pumped passively Q-switched solid-state laser (CryLaS, FTSS355-Q2, 355 nm, 1.1 ns). The emission spectra were recorded using the USB 2000+ Ocean Optics spectrometer. Pump powers were varied by moving the variable neutral density filter, and the pump spot size was 1.78×10^{-3} cm^2. The ASE/lasing measurements were all conducted in a nitrogen-filled glovebox.

UV–Vis Absorption Spectra: Absorption spectra of the 3D films were recorded using the PerkinElmer Spectrophotometer (Lambda 1050 UV/Vis/NIR) equipped with an integrating sphere.

Atomic Force Microscopy: The topographic images of 3D film before lamination and after delamination were obtained by atomic force microscopy using Nano Wizard II (JPK Instruments). The RMS (Root-Mean-Square) roughness was calculated using the free software (Gwyddion). The delamination was performed by peeling off the PEN substrate from the Glass substrate using a tweezer.

Scanning Electron Microscopy: Scanning Electron Microscopy (SEM) images of the Glass/3D films before lamination and after delamination were obtained by SUPRA 55 (Carl Zeiss) at 2 kV.

Grazing-Incidence Wide-Angle X-Ray Scattering: Grazing-Incidence Wide-Angle X-Ray Scattering (GIWAXS) patterns were acquired using the D8 Advance (BRUKER) in ambient. The X-ray incidence angle was varied from 0.1 to 0.4° to probe the crystalline properties at different depths of the films. The data analysis was conducted on the DIFFRAC. EVA software.

Photoluminescence Quantum Yield: PLQY was conducted on a homemade setup, equipped with a 405 nm CW laser diode (Thorlabs), an integrating sphere, an optical fiber, and a spectrometer (QE Pro, Ocean Insight). The samples were excited from glass side and the PLQY were obtained based on the standard three-step method. Pump power was scanned from 5 μW to 40 mW by changing the position of the neutral-density filter. To obtain a wide range of pump power density, the PLQY under unfocused (spot size, 4.12×10^{-2} cm^2) and focused (spot size, 8.82×10^{-4} cm^2) laser beam was both recorded.

TA and Streak Camera Measurement: The transient absorption was conducted on a custom-built setup equipped with a femtosecond laser source (PHAROS, Light conversion) and an optical parametric amplifier (Orpheus, Light conversion). All the fs-TA data were collected via exciting the sample from the PEN side with the 260 fs and 405 nm laser (0.5 μJ cm^{-2}), and the measurements were all conducted under vacuum. The PL_0 was recorded by a streak camera (Hamamatsu Universal C10910) equipped with a spectrometer (Acton SpectraPro SP2300), and the third harmonic of the amplifier (Light Conversion, Pharos/Hiro, 260 fs, 1030 nm, 1 kHz) were adopted as the excitation laser. Full details can be found in a previous publication.[17]

Supporting Information

Supporting Information is available from the Wiley Online Library or from the author.

Conflict of Interest

The authors declare no conflict of interest.

Author Contributions

Y.L. and U.W.P had the idea for this project and conceived the experiment. Y.L. fabricated the samples and conducted the film characterization and modeling. J.R. performed the lamination process. Y.L. and I.A. performed the in-depth ASE/lasing characterization. J.C.F. conducted the GIWAXS measurement and data analysis. Q.J. performed SEM measurement and the investigation on the heterostructure interface. All the authors contributed to the discussion and data analysis. Y.L., I.A.H., and U.W.P. wrote the manuscript with inputs from all the others. U.L., I.A.H., and U.W.P. supervised this project.

Data Availability Statement

The data that support the findings of this study are available from the corresponding author upon reasonable request.

[1] a) H. S. Kim, C. R. Lee, J. H. Im, K. B. Lee, T. Moehl, A. Marchioro, S. J. Moon, R. Humphry-Baker, J. H. Yum, J. E. Moser, M. Grätzel, N. G. Park, *Sci. Rep.* **2012**, *2*, 591; b) G. Xing, N. Mathews, S. S. Lim, N. Yantara, X. Liu, D. Sabba, M. Grätzel, S. Mhaisalkar, T. C. Sum, *Nat. Mater.* **2014**, *13*, 476; c) B. R. Sutherland, S. Hoogland, M. M. Adachi, P. Kanjanaboos, C. T. O. Wong, J. J. McDowell, J. Xu, O. Voznyy, Z. Ning, A. J. Houtepen, E. H. Sargent, *Adv. Mater.* **2015**, *27*, 53; d) B. R. Sutherland, E. H. Sargent, *Nat. Photon.* **2016**, *10*, 295; e) L. Lei, Q. Dong, K. Gundogdu, F. So, *Adv. Funct. Mater.* **2021**, *31*, 2010144.

[2] a) Y. Jia, R. A. Kerner, A. J. Grede, A. N. Brigeman, B. P. Rand, N. C. Giebink, *Nano Lett.* **2016**, *16*, 4624; b) P. Brenner, M. Stulz, D. Kapp, T. Abzieher, U. W. Paetzold, A. Quintilla, I. A. Howard, H. Kalt, U. Lemmer, *Appl. Phys. Lett.* **2016**, *109*, 141106; c) G. L. Whitworth, J. R. Harwell, D. N. Miller, G. J. Hedley, W. Zhang, H. J. Snaith, G. A. Turnbull, I. D. Samuel, *Opt. Express* **2016**, *24*, 23677.

[3] a) F. Deschler, M. Price, S. Pathak, L. E. Klintberg, D.-D. Jarausch, R. Higler, S. Hüttner, T. Leijtens, S. D. Stranks, H. J. Snaith, M. Atatüre, R. T. Phillips, R. H. Friend, *J. Phys. Chem. Lett.* **2014**, *5*, 1421; b) V.-C. Nguyen, H. Katsuki, F. Sasaki, H. Yanagi, *Appl. Phys. Lett.* **2016**, *108*, 261105.

[4] a) Q. Zhang, S. T. Ha, X. Liu, T. C. Sum, Q. Xiong, *Nano Lett.* **2014**, *14*, 5995; b) Q. Liao, K. Hu, H. Zhang, X. Wang, J. Yao, H. Fu, *Adv. Mater.* **2015**, *27*, 3405.

[5] C. Qin, A. S. D. Sandanayaka, C. Zhao, T. Matsushima, D. Zhang, T. Fujihara, C. Adachi, *Nature* **2020**, *585*, 53.

[6] H. Zhu, Y. Fu, F. Meng, X. Wu, Z. Gong, Q. Ding, M. V. Gustafsson, M. T. Trinh, S. Jin, X. Y. Zhu, *Nat. Mater.* **2015**, *14*, 636.

[7] J. Yang, Z. Liu, F. Zeng, M. Pi, T. Shi, Y. Bian, X. Tang, J. Du, W. Liu, Y. Leng, *Sol. RRL* **2019**, *3*, 1900127.

[8] Y. F. Jia, R. A. Kerner, A. J. Grede, B. P. Rand, N. C. Giebink, *Nat. Photon.* **2017**, *11*, 784.

[9] H. Kim, K. Roh, J. P. Murphy, L. Zhao, W. B. Gunnarsson, E. Longhi, S. Barlow, S. R. Marder, B. P. Rand, N. C. Giebink, *Adv. Optical Mater.* **2020**, *8*, 1901297.

[10] a) C. Zou, Y. Liu, D. S. Ginger, L. Y. Lin, *ACS Nano* **2020**, *14*, 6076; b) L. Zhao, K. Roh, S. Kacmoli, K. Al Kurdi, X. Liu, S. Barlow, S. R. Marder, C. Gmachl, B. P. Rand, *Adv. Mater.* **2021**, *33*, 2104867; c) H. Kim, L. Zhao, J. S. Price, A. J. Grede, K. Roh, A. N. Brigeman, M. Lopez, B. P. Rand, N. C. Giebink, *Nat. Commun.* **2018**, *9*, 4893.

[11] a) C. Cho, T. Antrack, M. Kroll, Q. An, T. R. Barschneider, A. Fischer, S. Meister, Y. Vaynzof, K. Leo, *Adv. Sci.* **2021**, *8*, 2101663; b) W. B. Gunnarsson, B. P. Rand, *APL Mater.* **2020**, *8*, 030902.

[12] a) H. Kroemer, *Proc. IEEE* **1963**, *51*, 1782; b) N. Holonyak, R. Kolbas, R. Dupuis, P. Dapkus, *IEEE J. Quantum Electron.* **1980**, *16*, 170; c) T. Numai, *Fundamentals of Semiconductor Lasers*, Springer, Kusatsu, Japan **2015**.

[13] a) M. Yuan, L. N. Quan, R. Comin, G. Walters, R. Sabatini, O. Voznyy, S. Hoogland, Y. Zhao, E. M. Beauregard, P. Kanjanaboos, Z. Lu, D. H. Kim, E. H. Sargent, *Nat. Nanotechnol.* **2016**, *11*, 872; b) N. Wang, L. Cheng, R. Ge, S. Zhang, Y. Miao, W. Zou, C. Yi, Y. Sun, Y. Cao, R. Yang, Y. Wei, Q. Guo, Y. Ke, M. Yu, Y. Jin, Y. Liu, Q. Ding, D. Di, L. Yang, G. Xing, H. Tian, C. Jin, F. Gao, R. H. Friend, J. Wang, W. Huang, *Nat. Photon.* **2016**, *10*, 699; c) M. Kaiser, Y. Li, I. Allegro, B. S. Richards, U. W. Paetzold, I. A. Howard, *Adv. Mater. Interfaces* **2021**, *8*, 2101326.

[14] G. E. Eperon, M. T. Horantner, H. J. Snaith, *Nat. Rev. Chem.* **2017**, *1*, 0095.

[15] Q. Zhao, A. Hazarika, X. Chen, S. P. Harvey, B. W. Larson, G. R. Teeter, J. Liu, T. Song, C. Xiao, L. Shaw, M. Zhang, G. Li, M. C. Beard, J. M. Luther, *Nat. Commun.* **2019**, *10*, 2842.

[16] a) A. Mohapatra, N. Singh, A. Singh, C.-Y. Lee, Y.-J. Lu, Y.-T. Tao, C.-H. Lee, C. W. Chu, *ACS Appl. Energy Mater.* **2021**, *4*, 1962; b) S. P. Dunfield, D. T. Moore, T. R. Klein, D. M. Fabian, J. A. Christians, A. G. Dixon, B. Dou, S. Ardo, M. C. Beard, S. E. Shaheen, J. J. Berry, M. F. A. M. van Hest, *ACS Energy Lett.* **2018**, *3*, 1192; c) W. A. Dunlap-Shohl, T. Li, D. B. Mitzi, *ACS Appl. Energy Mater.* **2019**, *2*, 5083; d) R. Schmager, J. Roger, J. A. Schwenzer, F. Schackmar, T. Abzieher, M. Malekshahi Byranvand, B. Abdollahi Nejand, M. Worgull, B. S. Richards, U. W. Paetzold, *Adv. Funct. Mater.* **2020**, *30*, 1907481.

[17] Y. Li, I. Allegro, M. Kaiser, A. J. Malla, B. S. Richards, U. Lemmer, U. W. Paetzold, I. A. Howard, *Mater. Today* **2021**, *49*, 35.

[18] a) P. Andrew, H. E. Madeline, Q.-B. Rafael, M. Arup, O. K. Shana, A. de Filippo, D. S. Gregory, H. S. Edward, *Proc. SPIE* **2019**, *11084*, 11084G; b) T. He, S. Li, Y. Jiang, C. Qin, M. Cui, L. Qiao, H. Xu, J. Yang, R. Long, H. Wang, M. Yuan, *Nat. Commun.* **2020**, *11*, 1672.

[19] M. Hammer, *1-D mode solver for dielectric multilayer slab waveguides*, https://www.siio.eu/oms.html.

[20] N. Pourdavoud, T. Haeger, A. Mayer, P. J. Cegielski, A. L. Giesecke, R. Heiderhoff, S. Olthof, S. Zaefferer, I. Shutsko, A. Henkel, D. Becker-Koch, M. Stein, M. Cehovski, O. Charfi, H. H. Johannes, D. Rogalla, M. C. Lemme, M. Koch, Y. Vaynzof, K. Meerholz, W. Kowalsky, H. C. Scheer, P. Gorrn, T. Riedl, *Adv. Mater.* **2019**, *31*, 1903717.